

**Tubular-body theory for viscous flows:  
Supplementary Material**

Lyndon Koens<sup>a</sup>

*Department of Mathematics & Statistics,  
Macquarie University, Sydney, NSW 2113, Australia and  
Department of Physics & Mathematics,  
University of Hull, Hull HU6 7RX, UK*

(Dated: February 9, 2022)

---

<sup>a</sup> lyndon.koens@mq.edu.au, L.M.Koens@hull.ac.uk

## EXACT SOLUTIONS TO TBT

In this section we outline how to construct exact solutions to the TBT integral equations. Exact solutions to Fredholm integral equations, like TBT, can be expressed through a function called a resolvent [1]. Hence the general solution to Eqs. (23) and (24) can be written as

$$\mathbf{f}(s, \theta) = \mathbf{M}_A^{-1} \cdot \left[ \mathbf{q}(s, \theta) - \langle \mathbf{M}_A^{-1} \rangle_{\theta}^{-1} \cdot \int_{-1}^1 ds' \mathbf{R}(s, s') \cdot \langle \mathbf{M}_A^{-1} \cdot \mathbf{q}(s, \theta) \rangle_{\theta} \right], \quad (1)$$

where  $\mathbf{R}(s, s')$  is resolvent. There are many ways to construct the resolvent [1] with the most general way being the method of Fredholm determinates. This method expresses the resolvent as

$$\mathbf{R}(s, s') = \left[ \sum_{n=0}^{\infty} \frac{\mathbf{A}_n(s, s')}{n!} \right] / \left[ \sum_{m=0}^{\infty} \frac{B_m}{m!} \right] \quad (2)$$

where  $B_0 = 1$ ,

$$\langle \mathbf{M}_A^{-1}(s) \rangle_{\theta}^{-1} \cdot \mathbf{A}_0(s, s') = \left( \frac{\mathbf{I}}{|\tilde{\mathbf{R}}|} + \frac{\mathbf{R}_0 \mathbf{R}_0}{|\tilde{\mathbf{R}}|^3} \right), \quad (3)$$

$$\begin{aligned} \langle \mathbf{M}_A^{-1}(s) \rangle_{\theta}^{-1} \cdot \mathbf{A}_n(s, s') = B_n \left( \frac{\mathbf{I}}{|\tilde{\mathbf{R}}(s, s')|} + \frac{\mathbf{R}_0(s, s') \mathbf{R}_0(s, s')}{|\tilde{\mathbf{R}}(s, s')|^3} \right) \\ - n \int_{-1}^1 dt \left( \frac{\mathbf{I}}{|\tilde{\mathbf{R}}(s, t)|} + \frac{\mathbf{R}_0(s, t) \mathbf{R}_0(s, t)}{|\tilde{\mathbf{R}}(s, t)|^3} \right) \cdot \mathbf{A}_{n-1}(t, s'), \end{aligned} \quad (4)$$

$$B_n = \int_{-1}^1 ds Tr[\mathbf{A}_n(s, s)], \quad (5)$$

$Tr[\cdot]$  denotes the trace and we have explicitly included the functional dependence for clarity. These series are guaranteed to converge and so provides an exact solution to the tubular-body problem in terms of a series of embedded integrals. In practice these integrals cannot be evaluated analytically and so it is often easier to invert the integral operator numerically.

## DETAILED DESCRIPTION OF THE NUMERICAL METHOD

This section provides a detailed description of the numerical method to solve the TBT equations from the text. This was done using a collocation process [1, 2]. In this process the arclength  $s \in [-1, 1]$  is divided in to  $M$  segments of constant length and  $\langle \mathbf{f}(s, \theta') \rangle_{\theta'}$  is assumed to be constant over each segment. We then choose to satisfy Eq. (23) at the centre

of each segment. This allows us to write Eq. (23) as

$$\begin{pmatrix} \langle \mathbf{M}_A^{-1} \cdot \mathbf{q} \rangle_\theta |_{s=s_1} \\ \langle \mathbf{M}_A^{-1} \cdot \mathbf{q} \rangle_\theta |_{s=s_2} \\ \vdots \\ \langle \mathbf{M}_A^{-1} \cdot \mathbf{q} \rangle_\theta |_{s=s_N} \end{pmatrix} = \begin{pmatrix} \mathbf{I} + \mathbf{K}_{s_1, s_1} & \mathbf{K}_{s_1, s_2} & \cdots & \mathbf{K}_{s_1, s_N} \\ \mathbf{K}_{s_2, s_1} & \mathbf{I} + \mathbf{K}_{s_2, s_2} & \cdots & \mathbf{K}_{s_2, s_N} \\ \vdots & \vdots & \ddots & \vdots \\ \mathbf{K}_{s_N, s_1} & \mathbf{K}_{s_N, s_2} & \cdots & \mathbf{I} + \mathbf{K}_{s_N, s_N} \end{pmatrix} \begin{pmatrix} \langle \mathbf{f}(s_1, \theta') \rangle_{\theta'} \\ \langle \mathbf{f}(s_2, \theta') \rangle_{\theta'} \\ \vdots \\ \langle \mathbf{f}(s_N, \theta') \rangle_{\theta'} \end{pmatrix}, \quad (6)$$

where  $2\Delta s$  is the size of each segment and

$$\mathbf{K}_{s_n, s_m} = \langle \mathbf{M}_A^{-1} \rangle_\theta \cdot \int_{s_m - \Delta s}^{s_m + \Delta s} ds' \left( \frac{\mathbf{I}}{|\tilde{\mathbf{R}}|} + \frac{\mathbf{R}_0 \mathbf{R}_0}{|\tilde{\mathbf{R}}|^3} \right) \Big|_{s=s_n}. \quad (7)$$

The solution to the above equation and  $\mathbf{K}_{s_n, s_m}$  integrals were determined in MATLAB [3] with  $M = 30$  throughout. A spline was then fitted through the  $\langle \mathbf{f}(s_i, \theta') \rangle_{\theta'}$  points with MATLAB's interpolate function and the result was used to determine  $\mathbf{f}(s, \theta)$  from Eq. (24). If the next  $\mathbf{f}_n(s, \theta)$  term is needed we evaluated  $\Delta \mathcal{L}[\mathbf{f}]$  at a collection of  $M \times M$  surface points using MATLAB's quad function and the results are interpolated. The speed of the evaluation is improved if the singularity in the two kernels are located at the same parametric point. This process is repeated to solve Eqs. (14) and (15) for the  $\mathbf{f}_n(s, \theta)$  terms till  $n = N$ . The approximation to the traction is then determined from Eq. (13) and the total force and torque determined in the normal way.

## TBT FOR A PROLATE SPHEROID

The simplest tubular body with known solutions is that of a spheroid. The resistance matrix of a spheroid is known exactly [4] and in the slender limit. For the sake of validation, we parametrised the surface of the spheroid as

$$\mathbf{S}_s(s, \theta) = \{s, \epsilon \rho(s) \cos(\theta), \epsilon \rho(s) \sin(\theta)\} \quad (8)$$

where  $\rho(s) = \sqrt{1 - s^2}$ , and we have used the Cartesian coordinates  $\{x, y, x\}$ , the resistance matrix for this spheroid can generally be expressed as

$$\begin{pmatrix} \mathbf{F} \\ \mathbf{L} \end{pmatrix} = \mu \begin{pmatrix} A & 0 & 0 & 0 & 0 & 0 \\ 0 & B & 0 & 0 & 0 & 0 \\ 0 & 0 & B & 0 & 0 & 0 \\ 0 & 0 & 0 & C & 0 & 0 \\ 0 & 0 & 0 & 0 & D & 0 \\ 0 & 0 & 0 & 0 & 0 & D \end{pmatrix} \begin{pmatrix} \mathbf{U} \\ \mathbf{\Omega} \end{pmatrix}. \quad (9)$$

where  $A$ ,  $B$ ,  $C$ , and  $D$  are the resistance coefficients related to motion. The exact form of these coefficients are given by

$$A = \frac{16\pi}{\phi + \chi_1}, \quad (10)$$

$$B = \frac{16\pi}{\phi + \epsilon^2 \chi_2}, \quad (11)$$

$$C = \frac{16\pi}{3\chi_2}, \quad (12)$$

$$D = 16\pi \frac{1 + \epsilon^2}{3(\chi_1 + \epsilon^2 \chi_2)}, \quad (13)$$

$$\phi = \int_0^\infty \frac{dx}{\sqrt{(1+x)(\epsilon^2+x)^2}}, \quad (14)$$

$$\chi_1 = \int_0^\infty \frac{dx}{(1+x)\sqrt{(1+x)(\epsilon^2+x)^2}}, \quad (15)$$

$$\chi_2 = \int_0^\infty \frac{dx}{(\epsilon^2+x)\sqrt{(1+x)(\epsilon^2+x)^2}}. \quad (16)$$

In the slender-limit,  $\epsilon \ll 1$  the these coefficients become

$$A = \frac{8\pi}{\log(4/\epsilon^2) - 1}, \quad (17)$$

$$B = \frac{16\pi}{\log(4/\epsilon^2) + 1}, \quad (18)$$

$$C = 0, \quad (19)$$

$$D = \frac{16\pi}{3(\log(4/\epsilon^2) - 1)}. \quad (20)$$

These results were calculated from the slender-body theory of Keller and Rubinow [5]. At this level of accuracy  $C = 0$ , though higher order corrections can be added to correct for this [6].

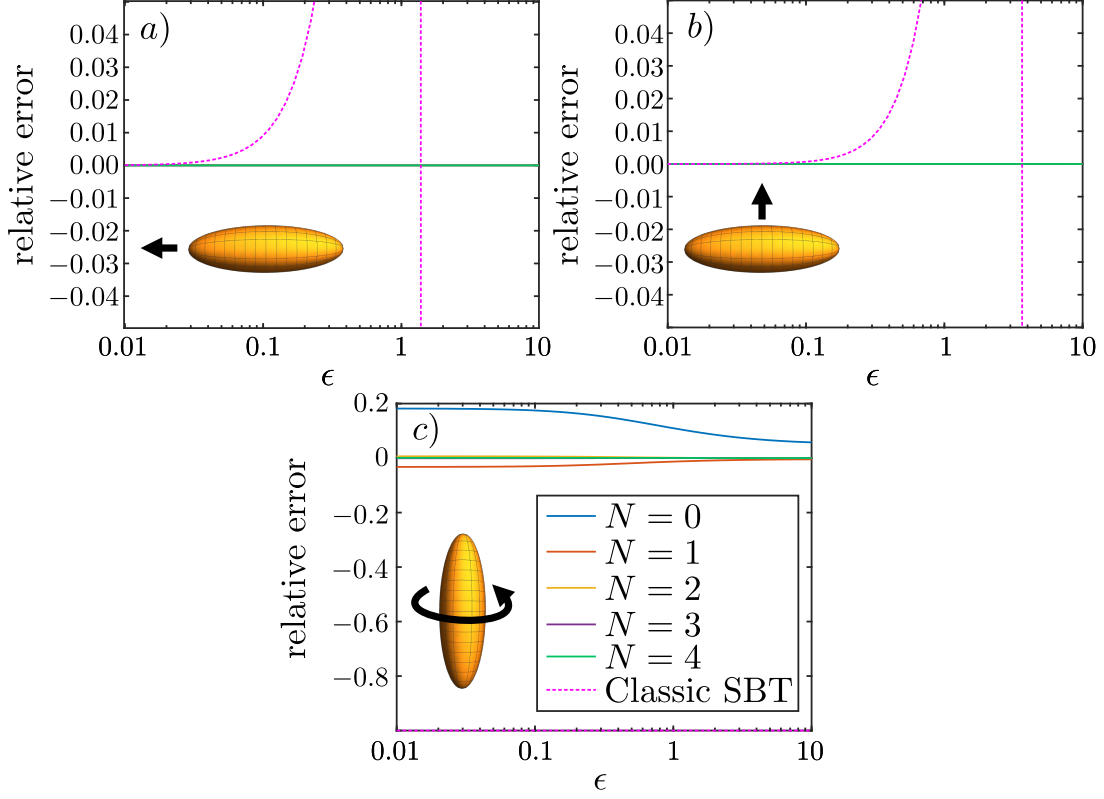


Figure 1. The relative error between TBT predictions and the exact resistance coefficients of a spheroid. The relative error is defined as the difference between the prediction and the exact coefficient, all divided by the exact coefficient. a) shows the relative error in the drag from axisymmetric translation. b) shows the relative error in the drag from non-axisymmetric translation. c) shows the relative error in the torque from axisymmetric rotation. Different lines correspond to the TBT prediction with different levels of truncation; blue is the leading term ( $N = 0$ ), red is the first two terms ( $N = 1$ ), yellow is the first three ( $N = 2$ ), purple is the first four ( $N = 3$ ), and green is the first five ( $N = 4$ ). The pink dashed line shows the relative error between the classic slender body theory prediction and the exact resistance coefficients.

The above results can be used to determine relative error between the exact solution and the solution from TBT for varying series truncation,  $N$ , and  $\epsilon$  (Fig. 1). In these plots we have included the relative error between the exact and the SBT results for reference. The non-axisymmetric rotation is provided in the main text. TBT is found to capture the drag from translation exactly for  $N = 0$ . This is because the exact solution for the drag on a spheroid was used as the local correction for the model. The predicted rotational coefficients,  $C$  and  $D$ , however differ for a  $N = 0$  series truncation with a maximum error of  $\approx 24\%$

around  $\epsilon = 1.2$  for the  $D$  coefficient and an  $\approx 20\%$  error for the  $C$  coefficient for small  $\epsilon$ . We note that classic SBT encounters a 100% error on  $C$  as it predicts  $C = 0$  at leading order. These errors decrease rapidly as  $N$  increases, with the predictions of  $C$  and  $D$  containing a maximum error of  $\approx 0.7\%$  for a series truncation of  $N = 2$  and  $N = 4$  respectively. These results have been shown over the range of  $\epsilon = [0.01, 10]$  (Fig. 1). The upper end of these results corresponds to an oblate spheroid with aspect ratio 10 and so is well beyond the typical slender-body theory limits (as demonstrated by the asymptotes in the SBT model lines). The error on the results are seen to be smooth and well behaved over this entire region, thereby indicating that TBT can work well beyond the SBT limits.

## TBT FOR A TORUS

Possibly the simplest wiry shape with a curved centreline is a torus. Similarly to the spheroid, the resistance matrix of a torus consists of four unique coefficients which can be again expressed as Eq. (9) for surface parametrisations of

$$\mathbf{S}_t(s, \theta) = \left\{ \epsilon \sin(\theta), \left( \frac{1}{\pi} - \epsilon \cos(\theta) \right) \cos(\pi s), \left( \frac{1}{\pi} - \epsilon \cos(\theta) \right) \sin(\pi s) \right\}. \quad (21)$$

The above torus parametrisation is scaled such that the arclength of the centerline equals 2 and so corresponds to a torus with a curvature of  $\pi$  and slenderness of  $\epsilon$ . Due to the rotational symmetries of this shape the resistance coefficients for the axisymmetric motions ( $A$ ,  $C$ ) can also be determined exactly [7–9]. These forms are complicated and so we omit them for brevity. Furthermore the resistance matrix has been determined in full in certain limits. Johnson and Wu [10] showed that for a slender torus the resistance coefficients are

$$A = \frac{16\pi}{2L + 1}, \quad (22)$$

$$B = 2\pi \frac{6L - 17}{(2L - 1)(L - 2) - 4}, \quad (23)$$

$$C = \frac{4}{\pi(L - 2)}, \quad (24)$$

$$D = \frac{8}{\pi(2L - 3)}, \quad (25)$$

where  $L = \log[8/(\pi\epsilon)]$ , while O’Neill *et al.* [11, 12] showed that in the limit of a closed torus ( $\epsilon = 1/\pi$ ) the coefficients become

$$A = 11.224, \quad B = 10.12, \quad C = 5.167, \quad D = 4.214. \quad (26)$$

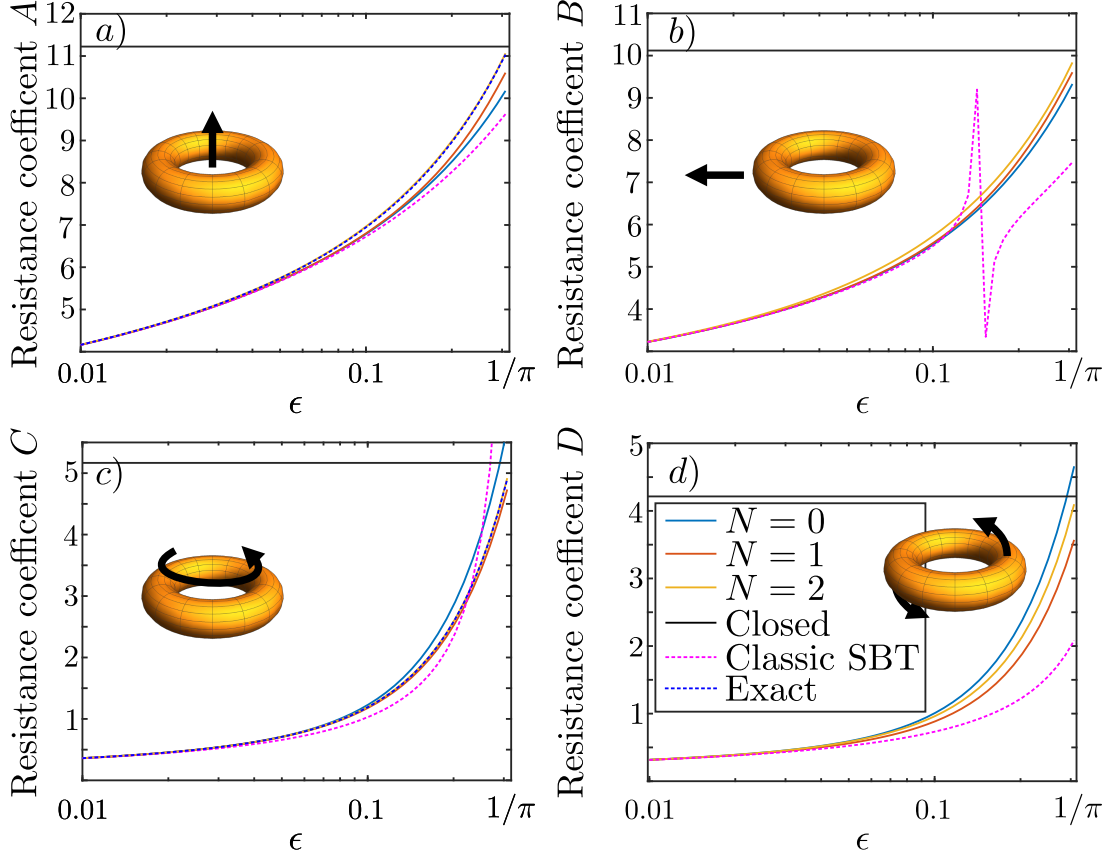


Figure 2. The resistance coefficients determined by TBT for a torus of radius  $1/\pi$  with thickness  $\epsilon$ . a) drag coefficient for axisymmetric translation,  $A$ ; b) drag coefficient for asymmetric translation,  $B$ ; c) drag coefficient for axisymmetric rotation,  $C$ ; d) drag coefficient for asymmetric rotation,  $D$ ; Blue lines correspond to TBT model with  $N = 0$ , Red is the TBT model with  $N = 1$ , and Yellow is the TBT model with  $N = 2$ . The black solid line represents the coefficients for a closed torus,  $\epsilon = 1/\pi$ , the pink dashed lines are the coefficients found with SBT and the blue dashed lines are the exact solutions (only available for axisymmetric motions). All lengths are scaled by half the arclength of the centreline.

We remind the reader that all the lengths have been scaled by half the arclength.

These results can be used to investigate the accuracy of the TBT model on curving bodies (Fig. 2) over the range of  $\epsilon \in [0.01, 1/\pi - 0.01]$ . We remind the reader that  $\epsilon = 1/\pi$  corresponds to a closed torus and is outside the typical SBT curvature restriction of  $\epsilon\kappa \ll 1$ . Over this entire region the TBT representation quickly converges to the solution, with small changes in the computed values for terms beyond a series truncation of  $N = 2$ . At this

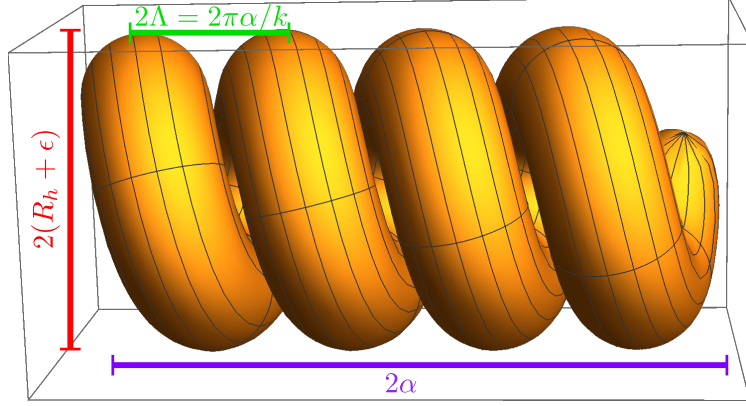


Figure 3. Diagram of a tightly wound helix. The axial length of this helix is given by  $2\alpha$  (purple), the helix pitch is  $2\Lambda$  (green), and the helix radius is  $R_h$  (red). The image shown is given by Eq. (27) with  $\epsilon = 0.5$ ,  $\Lambda = 1.1\epsilon$  and  $R_h = 1.5\epsilon$ .

level we find less than 1% error between the computed values and the exact solutions for the axisymmetric coefficients,  $A$  and  $C$  for all  $\epsilon$  tested. Furthermore the numerical results for the asymmetric resistance coefficients,  $B$  and  $D$ , can be seen to smoothly connect between the known limiting behaviours. This demonstrates the effectiveness of the TBT method on curved bodies.

## RESISTANCE MATRIX OF A TIGHTLY WOUND HELIX

The effectiveness of TBT can also be seen on a tightly wound helix (Fig. 3). Helices are iconic shapes in the viscous flows, due to their symmetries and their frequent appearance in biological and mechanical systems. Though common, little is known about how the dynamics of these helices change as they become tightly wound. One possible explanation of this is because such shapes lie well outside the SBT limits and so full numerical simulations would be needed. TBT however is exact and so allows us to investigate the behaviour in this limit.

We parametrise the surface of the helix as

$$\mathbf{S}_h(s, \theta) = \mathbf{r}_h(s) + \epsilon\sqrt{1 - s^{20}}\hat{\mathbf{e}}_\rho(s, \theta) \quad (27)$$

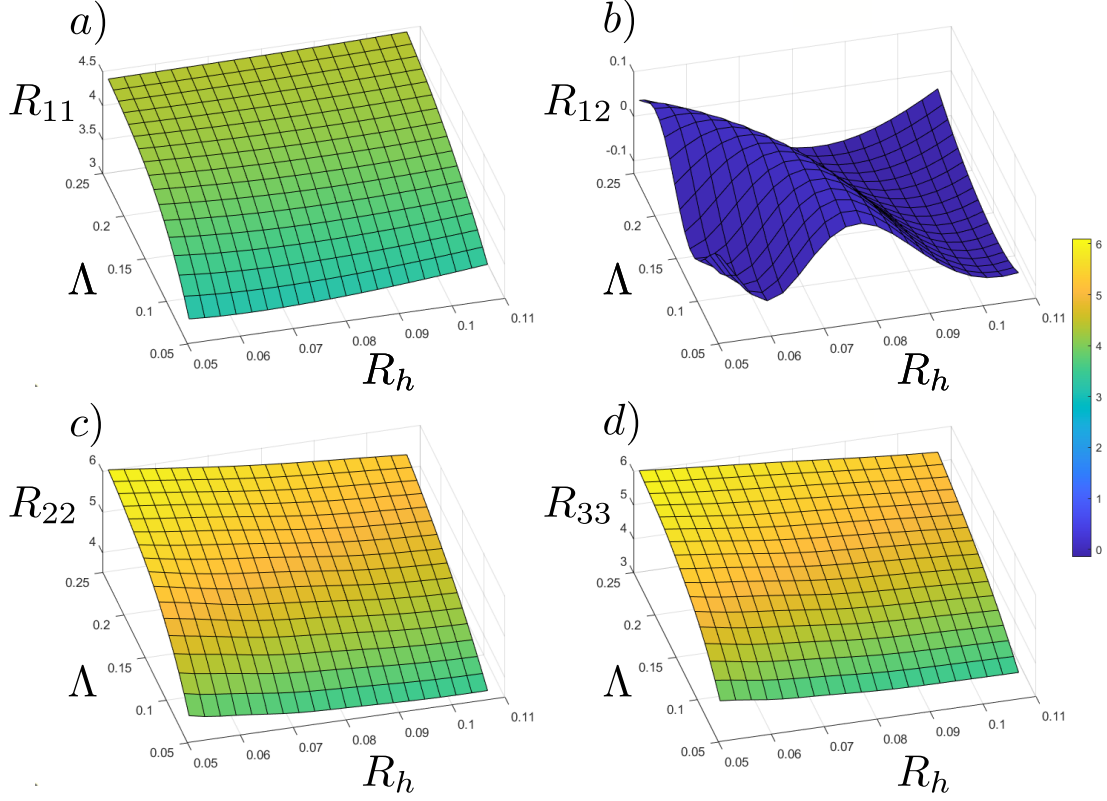


Figure 4. The non-zero components of resistance matrix relating translation and force for a tightly wound helix. a) Component  $R_{11}$ , b) Component  $R_{13}$ . c) Component  $R_{22}$ , d) Component  $R_{33}$ .

where

$$\mathbf{r}_h(s) = \{\alpha s, R_h \cos(ks), R_h \sin(ks)\}, \quad (28)$$

$$\hat{\mathbf{e}}_\rho(s, \theta) = \cos(\theta)\mathbf{d}_1(s) + \sin(\theta)\mathbf{d}_2(s), \quad (29)$$

$$\mathbf{d}_1(s) = \{kR_h \sin(\alpha ks), \cos(ks) \cos(\alpha ks) + \alpha \sin(ks) \sin(\alpha ks), \sin(ks) \cos(\alpha ks) - \alpha \cos(ks) \sin(\alpha ks)\}, \quad (30)$$

$$\mathbf{d}_2(s) = \{-kR_h \cos(\alpha ks), \cos(ks) \sin(\alpha ks) - \alpha \sin(ks) \cos(\alpha ks), \sin(ks) \sin(\alpha ks) + \alpha \cos(ks) \cos(\alpha ks)\}, \quad (31)$$

$\alpha$  is the cosine of the helix angle,  $R_h$  is the helix radius,  $k$  is the wave number and we have set the cross-sectional distribution of the helix to be  $\rho(s) = \sqrt{1-s^{20}}$  to provide a roughly constant cross-section that smoothly goes to 0 near the ends (Fig. 3). We note that  $\mathbf{d}_1(s)$ ,  $\mathbf{d}_2(s)$  and  $\hat{\mathbf{t}}(s)$  are perpendicular vectors chosen such that  $\partial_s \hat{\mathbf{e}}_\rho(s, \theta) = -\kappa \cos(\theta) \hat{\mathbf{t}}$  as required. The above helix has a curvature of  $\kappa = k^2 R_h$ , a torsion of  $\tau = \alpha k$  and is

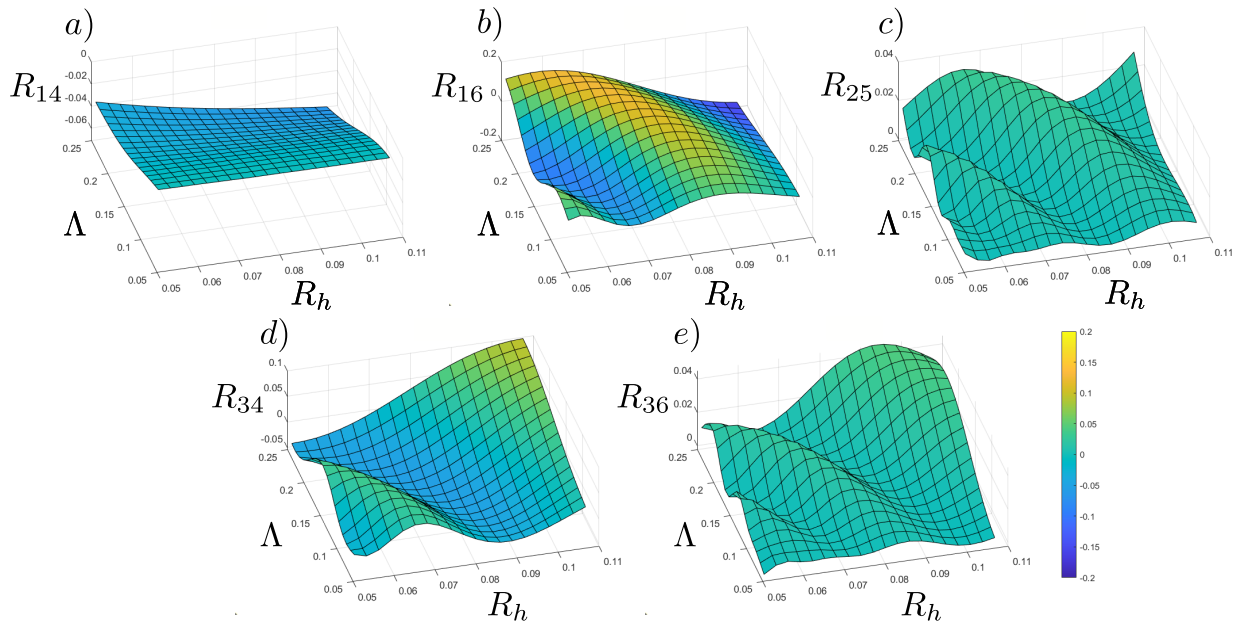


Figure 5. The non-zero components of resistance matrix relating rotation and force for a tightly wound helix. a) Component  $R_{14}$ , b) Component  $R_{16}$ , c) Component  $R_{25}$ , d) Component  $R_{34}$ , Component  $R_{36}$ .

parametrised by arclength so that  $\alpha^2 + k^2 R_h^2 = 1$ . There are two geometric restrictions on this geometry to ensure that the surface does not self intersect itself:  $2\pi\alpha/k > 2\epsilon$  and  $R_h > \epsilon$ . Since we wish to explore the behaviour of the helix near this limit we define the new parameter the helix pitch  $2\Lambda = 2\pi\alpha/k$  and will consider results for  $\Lambda \in (\epsilon, 5\epsilon]$  and  $R_h \in (\epsilon, 2\epsilon]$ . For all the simulations we use  $\epsilon = 0.05$  and  $N = 6$ . At this accuracy the results were found to have converged for all geometries considered.

This helical parametrisation produces 13 non-zero terms in the resistance matrix: four representing force from translation (Fig. 4), five representing the coupling between force and rotation or torque and translation (Fig. 5) and four representing torque from rotation (Fig. 6). In these plots we denote the  $i,j$ th component of the resistance matrix  $R_{ij}$ . Inspecting these coefficients we see that the diagonal terms of the resistance matrix displays a slow variation over this tightly coiled region. However the off diagonal terms display complex oscillatory behaviour that reduces as the body becomes closer to being closed. Even though this oscillation is small it can still significantly effect the motion and forces experienced by the body in different circumstances. For example the velocity of a force free helix undergoing unit rotation around its axis displays a strong oscillatory behaviour for motion perpendicular

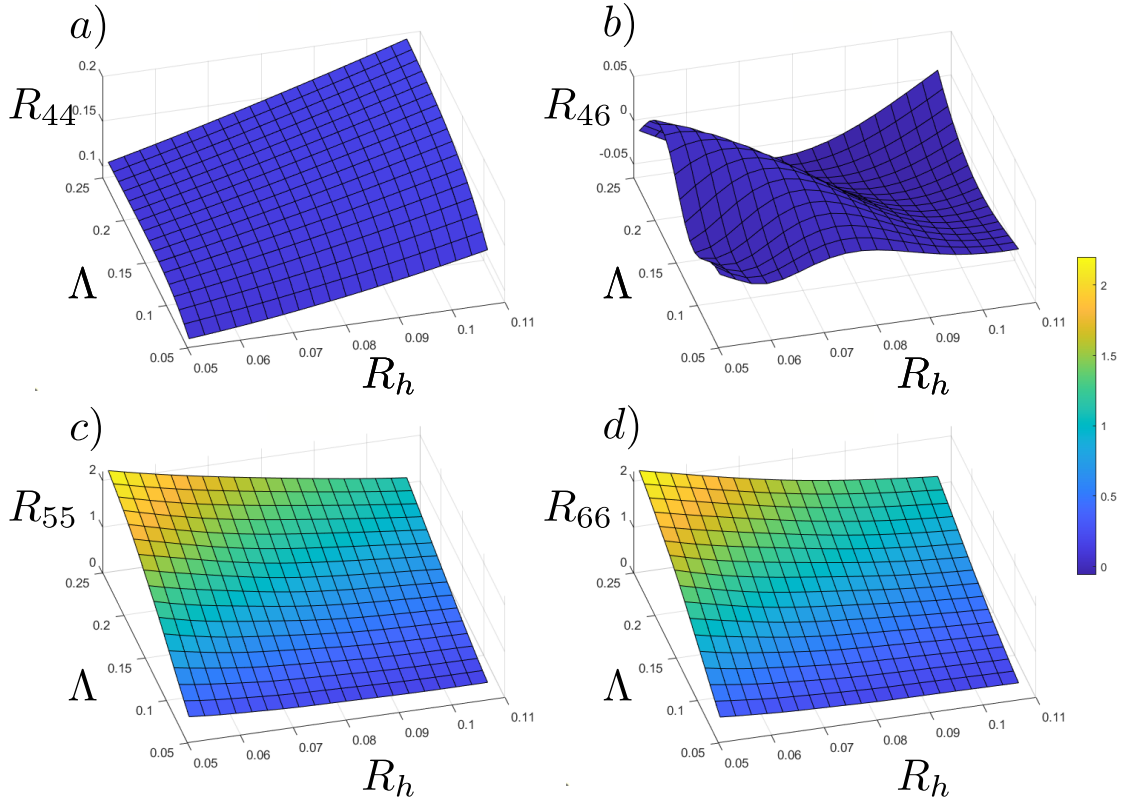


Figure 6. The non-zero components of resistance matrix relating rotation and torque for a tightly wound helix. a) Component  $R_{44}$ , b) Component  $R_{46}$ , c) Component  $R_{55}$ , d) Component  $R_{66}$ .

to the axis (Fig. 3b main text) and a small oscillation in the motion parallel to the axis when  $\Lambda \sim \epsilon$  (Fig. 3a main text). This further demonstrates the importance of models that can accurately resolve the behaviour beyond the SBT limits.

- 
- [1] A. D. Polianin and A. V. Manzhirov, *Handbook of integral equations*. Boca Raton, Florida: Chapman & Hall/CRC, 2nd ed., 2008.
  - [2] S. Kim and S. J. Karrila, *Microhydrodynamics: Principles and Selected Applications*. Boston: Courier Corporation, 2005.
  - [3] MATLAB, *version 9.10.0.1710957 (R2021a)*. Natick, Massachusetts: The MathWorks Inc., 2021.
  - [4] H. Lamb, *Hydrodynamics*. Cambridge: Cambridge University Press, 6th ed., 1932.
  - [5] J. B. Keller and S. I. Rubinow, “Slender-body theory for slow viscous flow,” *J. Fluid Mech.*,

- vol. 75, pp. 705–714, 1976.
- [6] L. Koens and E. Lauga, “The passive diffusion of *Leptospira interrogans*,” *Phys. Biol.*, vol. 11, p. 066008, 2014.
- [7] R. P. Kanwal, “Slow steady rotation of axially symmetric bodies in a viscous fluid,” *J. Fluid Mech.*, vol. 10, p. 17, 1961.
- [8] S. R. Majumdar and M. E. O’Neill, “On axisymmetric stokes flow past a torus,” *Zeitschrift für Angew. Math. und Phys. ZAMP*, vol. 28, pp. 541–550, 1977.
- [9] W. H. Pell and L. E. Payne, “On Stokes flow about a torus,” *Mathematika*, vol. 7, pp. 78–92, 1960.
- [10] R. E. Johnson and T. Y. Wu, “Hydromechanics of low-Reynolds-number flow. Part 5. Motion of a slender torus,” *J. Fluid Mech.*, vol. 95, pp. 263–277, 1979.
- [11] J. M. Dorrepaal, S. R. Majumdar, M. E. O’Neill, and K. B. Ranger, “A Closed Torus in Stokes Flow,” *Q. J. Mech. Appl. Math.*, vol. 29, pp. 381–397, 1976.
- [12] S. R. Majumdar and M. E. O’Neill, “Asymmetric stokes flows generated by the motion of a closed torus,” *Zeitschrift für Angew. Math. und Phys. ZAMP*, vol. 30, pp. 967–982, 1979.